Journal of CO2 Utilization 69 (2023) 102423

Contents lists available at ScienceDirect

Journal of CO2 Utilization

journal homepage: www.elsevier.com/locate/jcou

Electrochemical impedance analysis and degradation behavior of a Ni-GDC fuel electrode containing single cell in direct CO_2 electrolysis

Ifeanyichukwu D. Unachukwu [a,b], Vaibhav Vibhu [a,*], Jan Uecker [a,b], Izaak C. Vinke [a], Rüdiger-A. Eichel [a,b], L.G.J. (Bert) de Haart [a]

[a] Institute of Energy and Climate Research, Fundamental Electrochemistry (IEK-9), Forschungszentrum Jülich GmbH, 52425 Jülich, Germany
[b] Institute of Physical Chemistry, RWTH Aachen University, 52074 Aachen, Germany

ARTICLE INFO

Keywords:
Solid oxide electrolysis cells (SOECs)
CO_2-electrolysis, single cell performance
Degradation
Post-test analyses

ABSTRACT

The challenges of high degradation rate and significant carbon deposition, which are common with Ni-YSZ electrodes, have shifted attention to other electrode materials with enhanced performance in SOECs using carbon-containing fuels. In this study, the performance and electrochemical behavior of the Ni-GDC fuel electrode under CO_2 electrolysis were investigated. The study was performed over a range of operating conditions, varying the operating temperature, the CO_2 content of the fuel gas as well as the oxygen partial pressures in the oxygen electrode gas. Long-term stability test was performed up to 1070 h at 900 °C and a current density of −0.5 A·cm^{-2}. The electrochemical impedance spectra obtained from the various measurement were evaluated with DRT as well as an equivalent circuit model consisting of 4 time-constant; (LR-RQ1-RQ2-RQ3-Ws). The low frequency Warburg (short) element (Ws) was attributed to gas diffusion and surface processes at the fuel electrode, the mid frequency processes of RQ2 and RQ3 are assigned to the combined contribution of fuel and oxygen electrode. The high frequency RQ1 was assigned to the charge transfer process at the oxygen electrode. A low degradation rate of 31 mV·Kh^{-1} was observed during the long-term stability test. Furthermore, analysis of the degradation rate illustrates that significant contributions to the degradation were from the mid and high frequency processes, in addition to ohmic resistance. SEM analysis of the measured cell shows agglomeration of Ni particles, increase in electrode porosity as well as Ni migration away from the electrode/electrolyte interface.

1. Introduction

Climate change has emerged as one of the most pressing issues in politics and society as a whole. The emission of greenhouse gases, mostly CO_2, has reached its highest level in human history and is a significant contributor to global warming [1,2]. A significant fraction of these emissions originate from the chemical industries which either depend directly on or utilize products from fossil fuels [3]. Moreover, demand for petrochemical products by the chemical industries is expected to increase in the coming years. However, some of these chemical intermediates can be produced by utilizing CO gas. For example, the hydrolysis of methyl formate to produce formic acid and the catalytic carbonylation of methanol to produce acetic acid are some of the vital chemical processes that utilize CO as a building block [4]. As a result, rather than using fossil fuels in these processes, green technologies such as solid oxide electrolysis cells (SOECs) could be utilized to produce CO through CO_2 electrolysis. CO_2 gases from different industrial outputs could be electrochemically reduced to CO thereby reducing the overall industrial carbon emission [5,6].

Different competing green technologies are currently being investigated for CO production. Among the electrochemical CO_2 reduction possibilities, three technologies easily stand out; low temperature electrolysis, molten carbonate electrolysis and the SOECs. Of the three technologies, the SOEC is the most advanced technology for CO_2 electrolysis with years of operational hours [4]. In low temperature electrolysis, achieving high selectivity towards CO production is a non-trivial issue. Consequently, scarce catalysts such as IrO_2 and noble cathodes (Au and Ag) must be utilized. On the other hand, in molten carbonate electrochemical cell, the rapid corrosion of the electrolysis cell container remains a major challenge [4,7,8]. The SOEC technology, however, presents higher performance efficiencies at an industrially relevant scale. Therefore, with respect to the different indices of comparison such as the operating efficiency, faradaic efficiency, cell voltage, and area-specific resistance, the SOEC outperforms the molten

* Corresponding author.
E-mail address: v.vibhu@fz-juelich.de (V. Vibhu).

https://doi.org/10.1016/j.jcou.2023.102423
Received 20 September 2022; Received in revised form 1 February 2023; Accepted 2 February 2023
Available online 6 February 2023

carbonate and the low temperature electrolysis modes [4,7,8].

Despite the high efficiencies in SOECs, significant degradation, especially on the fuel electrode, has been observed. For example, considering the state-of-the-art Ni-YSZ fuel electrode materials, significant electrode degradation due to Ni migration and agglomeration has been reported [9–13]. Furthermore, noticeable degradation due to carbon deposition is observed when carbon-containing fuels are utilized [14–16]. Vanesa et al. [14] have investigated the formation of carbon on a Ni-YSZ electrode operating in fuel cell mode with a fuel mixture of 75% CO and 25% H_2 at 1073 K. They reported a pronounced carbon deposition on the Ni-YSZ electrode, resulting in an increase in polarization resistance, decrease in porosity and deactivation of the electrochemical activity. Similarly, He et al. [15] have investigated the extent of carbon formation on a Ni-YSZ pellet after four hours of exposure to humidified methane fuel gas at a temperature range of 773–1073 K. They observed extensive carbon formation on the Ni-YSZ pellet. The deposited carbon was observed to dissolve into the bulk of the Ni particles leading to significant expansion of the Ni-YSZ pellet. Such expansion could lead to delamination and deactivation of the electrode in single cells. Yuefeng et al. [17] demonstrated that the Ni-YSZ fuel electrode is deactivated in pure CO_2 electrolysis at 0.9 V and 700 °C. However, a better stable performance was observed at higher operating voltage of 1.3 V.

These issues, *i.e* carbon deposition and electrode deactivation, could be minimized or even resolved by using electrode materials that have mixed ionic and electronic conducting (MIEC) properties as well as suppress carbon deposition. The MIEC properties ensure that the electrochemical reactions extend beyond the three-phase boundary. Therefore, for these reasons, attention has shifted to ceria containing electrodes [7,15,18]. Under a reducing atmosphere, doped ceria oxide has MIEC properties, exhibiting a mixed-valence of Ce^{3+} and Ce^{4+}. As a consequence, the electrochemical reaction zone is extended from the three-phase boundary to the entire electrode surface. Furthermore, the electronic conductivity of ceria can partially compensate for Ni agglomeration and depletion thereby reducing the effect on performance [7]. With regards to carbon deposition, numerous works in literature have shown that the mixing of fuel electrode cermet with ceria reduces the amount of carbon deposition on the electrode [15,18–20]. For instance, He et al. [15] compared the amount of carbon deposition on Ni-YSZ pellet, with and without a ceria catalyst and observed less carbon on the pellet with a ceria catalyst than without a ceria catalyst. In general, the presence of localized electrons and oxygen vacancies in ceria electrodes has been observed to play a non-trivial role in preventing carbon deposition during CO_2 reduction [7,18–20]. In line with this, complete replacement of the YSZ oxide phase (in Ni-YSZ) with the GDC oxide phase (Ni-GDC) is being pursued.

In this work, the high temperature CO_2 electrolysis on solid oxide cells (SOC) consisting of a Ni-GDC fuel electrode is examined in detail. The electrochemical activity of the electrode is investigated by using electrochemical impedance spectroscopy (EIS) at different operating conditions. Impedance measurements were obtained at different compositions of CO_2 and CO, as well as at different temperatures (750–900 °C). Furthermore, a long-term stability test was performed to study the performance and durability of the electrode during operation. Finally, post-test analysis was carried out in order to understand the degradation behavior.

2. Experimental and methods

2.1. Preparation of the cells and electrodes

For the electrochemical measurements, electrolyte-supported single cells were fabricated. The fuel electrode is made of commercial NiO-$Ce_{0.9}Gd_{0.1}O_{0.95}$ (GDC) powder from Marion Technologies (NiO: GDC, 65:35 wt ratio), while the LSCF ($La_{0.58}Sr_{0.4}Co_{0.2}Fe_{0.8}O_{3-\delta}$) oxygen electrode powder was self-synthesized using a modified Pecheni method [21]. To prepare the electrode paste, NiO-GDC powder was mixed in a binder solution comprising 6 wt% ethyl cellulose (binder) dissolved in α-terpineol (dispersant). The slurry was then mixed using a planetary vacuum mixer (THINKY Mixer ARV-310) and subsequently homogenized for about 30 min by roll milling. A similar procedure was used to create the LSCF oxygen electrode slurry. Dense 8YSZ electrolyte supports from Kerafol® (d=20 mm, thickness 250 μm) were used to create the button cells. A thin layer (4–5 μm) of GDC was screen printed (EKRA screen printing Technologies) on one side of 8YSZ substrates and sintered at 1350 °C for 1 h under air to form a barrier layer for the oxygen electrode. After that, the fuel electrodes (15–18 μm) were screen printed on the opposite side of the electrolyte. Five different sintering temperatures were considered: 1150, 1200, 1250, 1300, and 1350 °C for 2 h at a heating rate of 2 °C·min^{-1}. Based on the polarization resistance, 1200 °C for 2 h was chosen as an optimized sintering condition. The LSCF layer was screen printed on the GDC barrier layer side and subsequently sintered at 1080 °C for 3 h. Finally, a NiO layer screen printed on the fuel electrode side was used as a current collector. The single-cell configuration before reduction is represented by NiO-GDC/8YSZ/GDC/LSCF. Following the same procedure, NiO-YSZ electrode was also fabricated and sintered at 1350 °C for 4 h, which is the optimized sintering condition for this electrode.

2.2. Electrochemical measurement set-up and procedures

For the electrochemical measurement, a two-electrode (four-wire) NorEcs Probostat™ set-up was used in the characterization of the single cells [22]. The cell was heated up to 900 °C (with 1 °C·min^{-1}), after which the nickel oxide cermet (NiO-GDC) was gradually reduced to nickel (Ni-GDC) as described by Foit et al. [23]. Following the reduction, IviumStat (Ivium Technologies) potentiostat/galvanostat devices were used to acquire the impedance spectra as well as the current density-voltage characteristics. The frequency range during the impedance measurement was varied from 110 kHz to 0.11 Hz with an AC amplitude of 50 mV and 21 frequencies per decade. Similarly, the current density-voltage (I-V) characteristics were obtained as previously described [23]. The quality of the impedance spectra was analyzed and validated through the Kramers Kronig transformation test [24]. Impedance measurements were taken at OCV under various temperature ranges (750–900 °C) and CO_2 partial pressures. Long-term stability tests of the button cells were carried out at 900 °C with a current density of −0.5 A·cm^2 for 1070 h. Impedance spectra were analyzed with both the complex non-linear least-square (NLLS) method as well as the distribution of relaxation times (DRT) transformation. A commercially available NLLS-fit program (RelaxIS® software, RHD-Instruments) was utilized in the fitting procedure and the DRT transformations.

2.3. Post-test analysis

The morphology of the cells was examined with Quanta FEG 650 (FEI©) scanning electron microscope.

3. Results and discussion

3.1. Sintering temperature optimization (SEM and impedance)

Single cells of NiO-GDC were fabricated and analyzed based on their sintering temperature. Five different sintering temperatures were considered; 1150, 1200, 1250, 1300 and 1350 °C for 2 h. However, a tape test was performed on the electrodes showed that the electrodes sintered at 1150 °C showed poor adhesion to the electrolyte, hence it was not considered for the rest of the measurement. Fig. 1a-d shows the SEM images of the cell before the reduction process. The SEM images clearly show an increase in particle agglomeration with the increase in sintering temperature. The cell sintered at 1350 °C exhibits the most pronounced particle agglomeration while the 1200 °C sintered cell

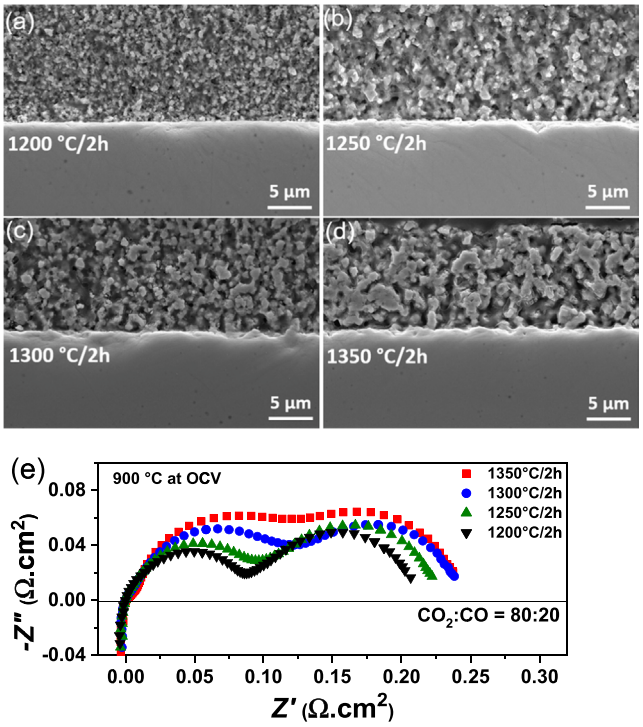

Fig. 1. SEM images of the Ni-GDC electrode layers on 8YSZ substrates sintered at a) 1200 °C, b) 1250 °C, c) 1300 °C, d) 1350 °C, and e) the impedance spectra of the corresponding single cells comprising Ni-GDC fuel electrode at OCV.

shows the least particle growth. Fig. 1e shows the impedance spectra of the cells obtained at 900 °C under OCV conditions. A decrease in polarization resistance (R_p) with decreasing sintering temperature is observed and the lowest R_p is observed for the cell sintered at 1200 °C. The result agrees with the microstructural observation from the SEM. An increase in particle agglomeration observed at higher sintering temperatures results in a decrease in the electrode surface area and thus, a decrease in the electrochemical reaction zone. Consequently, an increase in R_p is observed with increased particle agglomeration [25]. Optimized cells, sintered at 1200 °C were further used for the electrochemical characterization and the long-term degradation test.

3.2. Electrochemical characterization

3.2.1. Cell performance

To characterize the cell performance, I-V characteristics as well as impedance measurements were compared to those of conventional Ni-YSZ cells. Fig. 2a compares the I-V characteristics of electrolyte-supported single cells containing Ni-GDC and Ni-YSZ fuel electrodes, respectively. Both single cells were prepared using 8YSZ electrolyte support with an LSCF oxygen electrode and measured in the same test rig. It can be seen that the Ni-GDC electrode containing single cell exhibits a higher current density of − 1.16 A cm^{-2} compared to the Ni-YSZ cell (−0.63 A cm^{-2}) at 1.5 V and 900 °C. Fig. 2b shows the Nyquist plots obtained from the Ni-GDC cell in comparison to that of the Ni-YSZ cell. For the Ni-GDC cell, a lower R_p value of 0.23 Ω.cm^2 is observed compared to the 0.44 Ω.cm^2 observed for the Ni-YSZ cell at 900 °C. The higher performance of the Ni-GDC could be attributed to the enhanced electrochemical properties of the GDC as a result of the MIEC property [26–29].

Further I-V measurements were obtained for the Ni-GDC cell under varying operating temperatures. Fig. 2c shows the I-V characteristics of the cell as a function of operating temperature (750–900 °C). The current density increases with an increase in temperature. Such a trend is expected due to the enhancement of electrochemical kinetics at higher

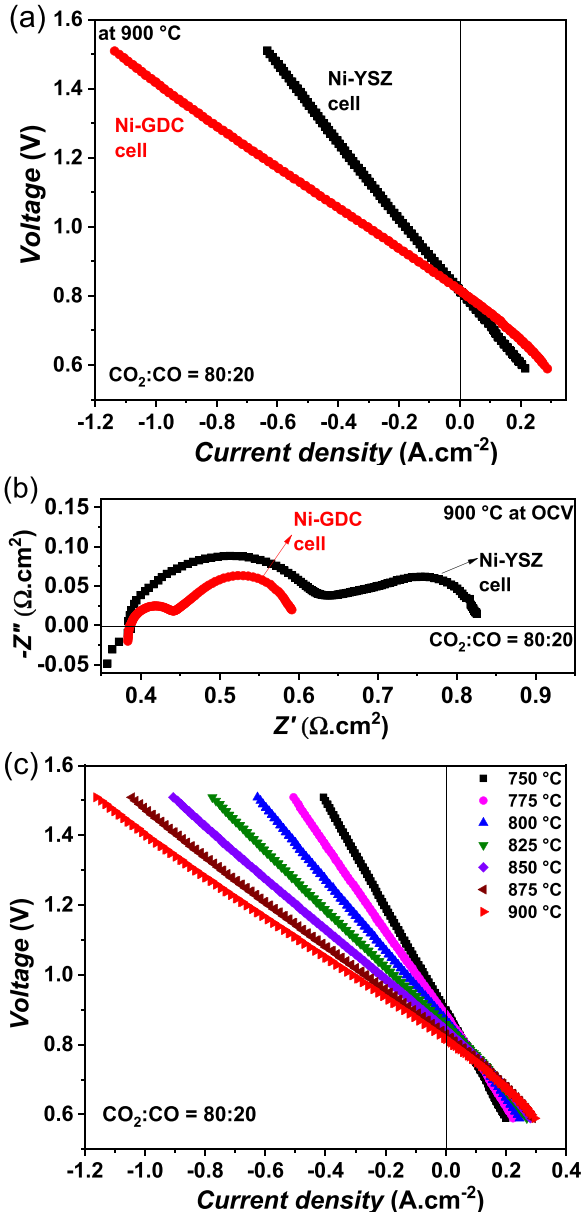

Fig. 2. (a) Comparison of current-voltage characteristics between Ni-GDC and Ni-YSZ electrode containing single cells, (b) Nyquist plots, and (c) I-V characteristics of Ni-GDC cell as a function of temperature with 80% CO_2 and 20% CO feed gas mixture.

operating temperatures. A maximum current density of − 1.16 A cm^{-2} is observed at 1.5 V and 900 °C. The continuity of the I-V curves across the OCV indicates that the Ni-GDC fuel electrodes can function as reversible SOCs [13]. In most of the cell measurements, the observed open circuit voltage was within 10 mV of the theoretical open circuit voltage according to the Nernst equation, which indicates sufficient cell sealing.

3.2.2. Electrochemical process identification

3.2.2.1. Measurement at different temperatures. To investigate thermally activated processes, impedance spectra were obtained and analyzed at different temperatures from 750° to 900°C in both OCV conditions as well as under polarization. Fig. 3a illustrates the Nyquist plots as a function of temperature at OCV. Two distinct arcs are easily identified in the impedance spectra; a low and a high frequency arc. While the low

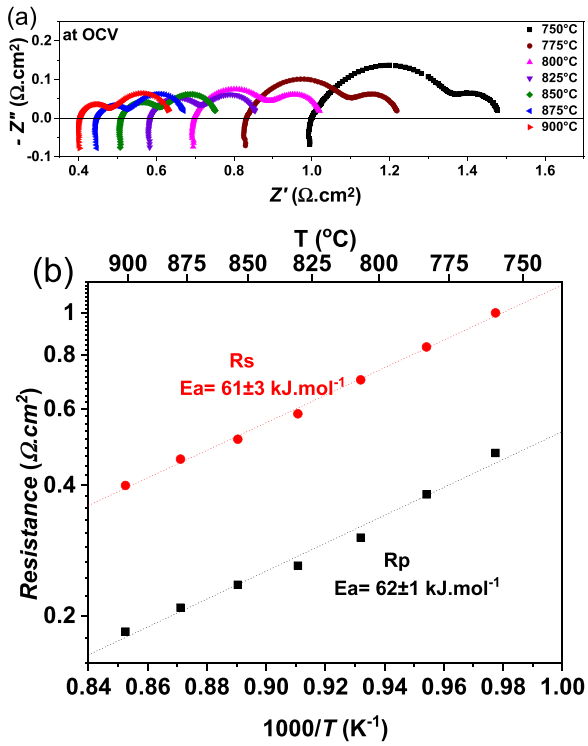

Fig. 3. a) Variation of impedance spectra with temperature, and (b)Arrhenius plot of the ohmic (R_s) and polarization resistance (R_p) for the single cell containing Ni-GDC fuel electrode at OCV.

frequency arc is relatively unchanged with temperature variation, the high frequency arc shows a pronounced increase in magnitude with the decrease in temperature. This suggests that the high frequency electrochemical processes are thermally activated processes. Similar trend was also recorded under polarization (as shown in supplementary Fig. S1). In general, the decrease in temperature, from 900° to 750°C, caused an increase in the real and imaginary contributions in the Nyquist diagram of the impedance spectra. Such an increase is attributed to the reduction of ionic conductivity and electrochemical reaction kinetics in the electrodes with decreased temperature. The ohmic resistance (R_s) of the cell is determined from the intercept with the real axis at the high frequency in the Nyquist plot. Consequently, the activation enthalpy of the ohmic resistance is calculated from the slope of the Arrhenius equation as represented in Eq. (1) and illustrated in Fig. 3b. The determined value of 61 kJ/mol is consistent with the values of ionic conductivity of the 8YSZ electrolyte [30].

$$\ln R = -\ln\sigma_0 + \frac{E_A}{R_g T} \quad (1)$$

The impedance spectra were analyzed with both the DRT transformation and the NLLS method. Fig. 4a shows the DRT representation of the impedance spectra as a function of temperature. Five peaks (P1, P2, P3, P4 and P4a) are observed in the DRT plot within the measured frequency range of 0.11 Hz to 110 kHz. The impedance spectra, however, were modeled with an equivalent circuit consisting of four time constants in series to a resistor and an inductor (LR-RQ-RQ2-RQ3-Ws) as shown in Fig. 4b. Furthermore, a comparison was made between the simulation of the fit and measured data. The comparison shows good agreement between the DRT of the proposed ECM and the DRT of the measured data (Supplementary Fig. S3). Also, the error plot showed non-systematic distribution around the frequency axis, which indicates that the proposed ECM can effectively reproduce the obtained impedance data across the measured frequency range (Supplementary Fig. S3).

The time constants RQ1, RQ2 and RQ3 correspond to the processes

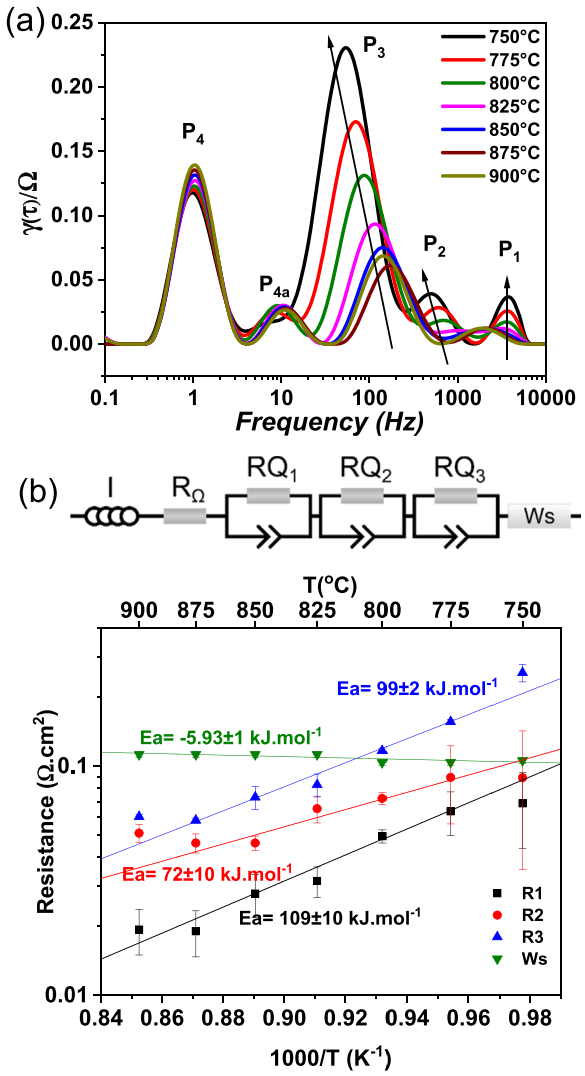

Fig. 4. a) DRT plot of the impedances as a function of temperature, (b) equivalent circuit model used in impedance fitting, and (c) Arrhenius plot of the resistances as a function of temperature.

P1, P2 and P3 on the DRT plot respectively. While the P4 peak corresponds to the infinite length Warburg short element (Ws) with the P4a peak interpreted as the satellite peak of the Ws [31,32]. The DRT reveals a significant dependence of the high/mid frequency peaks on temperature variation. P1, P2 and P3 exhibit an increase in magnitude with the decrease in temperature. On the other hand, P4 is almost independent of temperature variation. The measurements indicate that the mid frequency process (P3) dominates the electrode process at the lower temperature of 750 °C.

The absolute values of the resistances were obtained from the NLLS fitting of the impedance spectra with the equivalent circuit model depicted in Fig. 4b. Fig. 4c illustrates the Arrhenius plot of the determined resistances. The resistances R1, R2 and R3 corresponding to processes P1, P2 and P3 respectively, exhibit a significant increase with a decrease in operating temperature, while Ws is relatively unchanged with the decrease in temperature. The trend shows good agreement with the observed DRT plot. R1 and R3 exhibit high activation energies of 109 ± 10 kJ mol^{-1} and 99 ± 2 kJ mol^{-1}, respectively, while R2 shows an activation energy of 77 ± 10 kJ mol^{-1}.

Considering the electrochemical processes occurring in the electrode, different electrode reaction steps exhibit different temperature dependencies and these dependencies may identify the possible electrode process. For instance, gas diffusion processes exhibit an almost

independent temperature dependency while charge transfer processes and processes from the transfer of ionic species show strong temperature dependency and high activation energies [33–36].

3.2.2.2. Effect of fuel gas compositions. Measurements under different compositions of the CO_2 fuel gas were performed to further investigate the fuel electrode processes. The CO_2/CO ratio was systematically changed from 90/10–50/50. The impedance spectra as well as current-voltage characteristics were obtained as a function of CO_2/CO ratio. Fig. 5a illustrates the Nyquist plots obtained from the variation of CO_2 content at OCV. An increase in the amount of CO_2 in the fuel gas led to an increase in R_p. The mid and low frequency arcs exhibit a more pronounced dependence, increasing in magnitude with increasing CO_2 content. This observation is contrary to what is expected when fuel gas is increased. In fact, in CO_2 electrolysis mode at OCV conditions, there is lower electrochemical activity towards CO_2 reduction than CO oxidation, hence an increase in R_p is observed with increasing CO_2 content. Such observation could be attributed to preferential adsorption or higher activation energy of CO_2 desorption on the active catalyst sites of the oxide phase and Ni metal [23,37]. This result is in agreement with a similar experiment by Foit et al. [23] on CO_2 electrolysis in Ni-YSZ. They observed that the increase in CO_2 content in the fuel gas composition led to an increase in ASR at OCV conditions. However, at higher current densities, increasing the CO_2 gas compositions resulted in a decrease in ASR. They opined that at higher current densities, mass transport limitation dominates the overall reaction rate. Hence, decreasing the CO_2 content resulted in a lesser amount of fuel gas for reaction leading to a decrease in the electrochemical reaction.

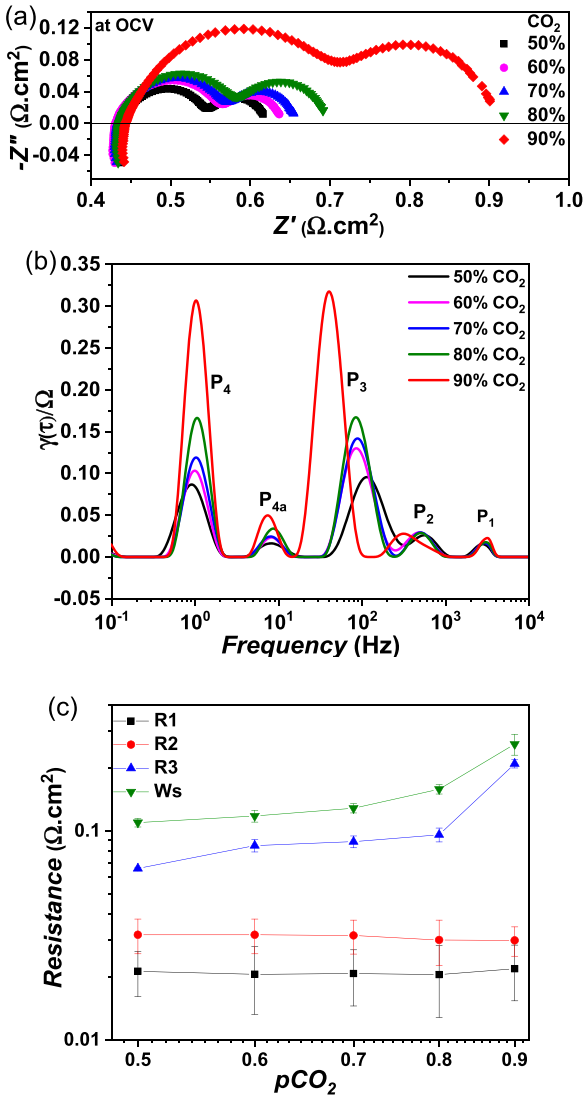

Fig. 5. a) Variation of impedance spectra, b) DRT plots, and (c) NLLS fitting plot of resistances, as a function CO_2 content.

The corresponding DRT plots of the impedance spectra are represented in Fig. 5b. Similar to the trend in the Nyquist plot, the low/mid frequency P4 and P3 peaks exhibit pronounced dependence on CO_2 variation while P1 and P2 peaks are relatively constant. This suggests that the underlying contributing processes of P4 and P3 peaks are most likely fuel electrode processes while P1 and P2 could be oxygen electrode contributions. Furthermore, the P4 and P3 peaks are observed to exhibit the highest contribution to the electrochemical impedance. Fig. 5c illustrates the obtained resistance from the fitting of the impedance spectra using the equivalent circuit model. The trend is in agreement with the observation in the DRT plot, wherein Ws and R3 resistances show a significant increase with an increase in CO_2 content. The significant CO_2 content dependence of the low frequency P4 peak as well as the observed independent temperature behavior indicates that this process is most likely a diffusion process [34,35,38]. However, the GDC cermets have been reported to show a low-frequency peak resulting from the chemical capacitance caused by the variation in the oxygen nonstoichiometry of the GDC electrode [38,39]. Therefore, the low frequency P4 peak is attributed mostly to a gas diffusion process and possible contribution from the oxygen nonstoichiometry of the GDC electrode.

Considering the frequency regime of the P3 process, reactions at the electrode/electrolyte interface can be ruled out since these processes typically exhibit high relaxation frequencies [33,40–42]. With a frequency range between 40 Hz and 250 Hz, this suggests a process towards the electrode sub-surface. Such mid frequency process could be attributed to gas-solid interaction such as adsorption, dissociation and desorption of the gas species [38]. Several authors [7,18,19] have attempted to suggest possible elementary mechanisms of CO_2 reduction on ceria containing cermets. Chueh et al. [18] investigated the surface electrochemistry of CO_2 reduction and CO oxidation on a ceria cermet. They opined that the electrochemical reduction of CO_2 to CO occurs via two single-electron transfer steps, with carbonate ($(CO_3)^{2-}$) formation as an intermediate process. The formed carbonate further absorbs and saturates the electrode surfaces thereby reducing the overall kinetics of CO_2 reduction. In general, the carbonate adsorption process is regarded as a major rate-determining step in CO_2 reduction [7,18,19]. Therefore, following the variation of temperature and CO_2 content, the P3 process has shown to exhibit the highest resistance and hence the rate-determining step in the CO_2 electrochemical reduction. Therefore, this process could be inferred to be related to an adsorption process. The mid frequency P3 peak is therefore attributed to a possible surface electrode reaction process (adsorption/desorption) of the gas species in addition to a charge transfer process on the electrode surface.

3.2.2.3. Effect of pO_2 variation on the oxygen electrode side. To investigate oxygen electrode processes, measurements under different partial pressures of oxygen (pO_2) were performed from 0.1 to 1 atm. The obtained impedance spectra were analyzed with both the DRT method and ECM fitting. Fig. 6a and b represent the DRT transformation and the ECM fitting of the impedance spectra as a function of pO_2 respectively. The P4 peak is independent of pO_2, while P3, P2 and P1 show very slight changes with pO_2 variation. From the DRT plot alone, it is arguable to attribute some of the peaks to the oxygen electrode process alone. However, this could indicate that the contribution of the oxygen electrode is minimal. The fitting results (Fig. 6b) of the impedance spectra with the equivalent circuit model showed that R1 (representing P1 peak) and R2 (P2 peak) resistances are mostly, contributions from oxygen electrode processes. However, following the inconsistency between the

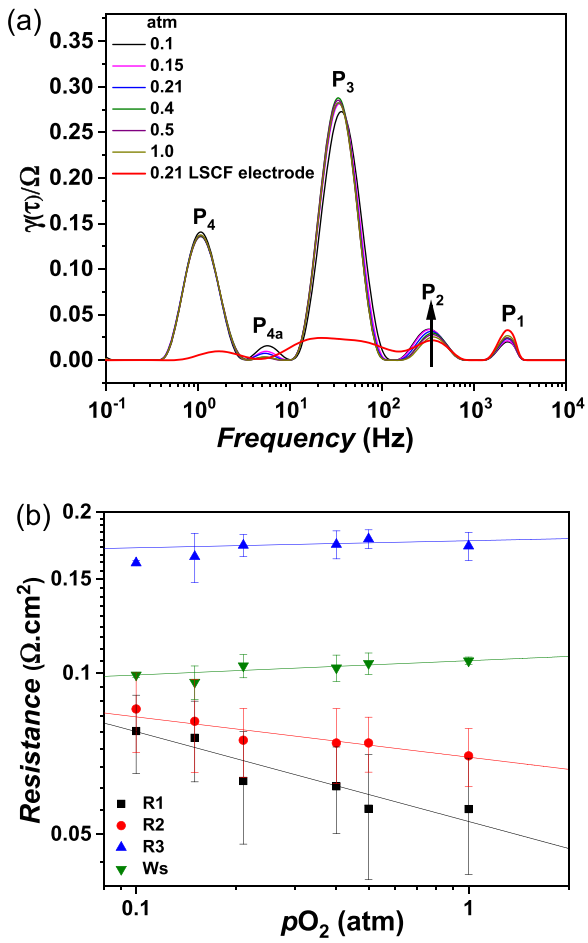

Fig. 6. a) DRT plot and (b) NLLS fitting plot of resistance as a function oxygen partial pressure.

DRT representation and the NLLS fitting of the impedance, a further experiment was necessary to clarify the impedance contribution from the oxygen electrode. For this, impedance measurement was performed on a symmetrical half-cell containing LSCF electrodes (in two-electrode measurements). The obtained DRT was compared in Fig. 6a. The comparison shows that the P1 and P2 peaks are essentially oxygen electrode processes while P3 and P4 are mainly fuel electrode resistance contributions with slight contributions from the oxygen electrode. This is in agreement with the observed trend in the NLLS fitting. However, the focus of the current study is on the fuel electrode processes, hence the electrochemical processes of the oxygen electrode were inferred from the numerous literature on LSCF electrodes [40–43]. Overall, the obtained DRT representation of the LSCF impedance spectra (with their corresponding frequency range) for symmetrical half-cell is in good agreement with literature observation. [40,42]. Chen et [42] al. investigated the performance of LSCF symmetrical cells with different fabrication methods. From their analysis, they ascribed the low frequency peak between 1 and 10 Hz to gas diffusion process, the mid frequency peak between 10 and 500 Hz to surface exchange and ion diffusion process (which corresponds to the P3 and P2 in this report) and lastly, a high frequency peak (around 1000 Hz) to charge transfer process across the interface. A similar result was also observed by Leonide et al. [40] in the impedance study of LSCF and LSF electrodes; a low frequency (0.3–10 Hz) gas diffusion process, a mid frequency (2–500 Hz) oxygen surface exchange process followed by oxide diffusion in the bulk of the electrode and lastly a high frequency charge transfer process were observed. Therefore, following the high activation energy of R1 (as shown in Fig. 4c) as well as the high frequency range of the P1 peak (similar to ref [40,42]), there is no doubt that this is in good agreement and coincides with the charge transfer process of the oxygen electrode. Table 1 summarizes the possible electrochemical process contribution related to the individual polarization resistances.

3.2.3. Degradation

Long term stability test were performed to investigate the performance stability of the cells during long operating times. The measurement was performed at 900 °C at a current density of − 0.5 A·cm^{-2} for up to 1070 h on two different cells with a fuel gas composition consisting of 80% CO_2 and 20% CO. Fig. 7a illustrates the degradation rate of the cell, represented as an increase in cell voltage as a function of time. The cell degradation was obtained by evaluating the slope of the curve. A degradation rate of 31 mV·kh^{-1} could be determined. In another cell, the evolution of the degradation mechanism was investigated during the long-term stability test by performing impedance measurements at OCV every 100 h. Fig. 7b and c illustrate the evolution of the impedance spectra as well as the ohmic (Rs) and polarization (R_p) resistances respectively as a function of operation time. The Rs increased from 0.48 to 0.53 Ω·cm^2 while the R_p increased from 0.28 to 0.35 Ω·cm^2 after the degradation test. It is known that the loss of electrode contact surface with the current collector could also lead to an increase in the ohmic resistance and thus an increase in degradation rate. Such ohmic resistance increase due to loss of contact surface is usually accompanied by a proportional increase in the R_p. However, in our case, the increase in R_p is higher and thus disproportionate to the ohmic resistance increase, indicating that ohmic resistance is most likely, not due to contact loss. Fig. 7d illustrates the equivalent circuit analysis of the spectra which shows that the degradation behavior is dominated by the high/mid frequency processes of R1, R2 and R3 while Ws is relatively unaffected. This implies that both the oxygen electrode and the fuel electrode contributed to the degradation mechanism.

3.3. Post-test characterization

Post-test analysis was performed on the measured cell to investigate the morphology and the microstructure of the electrodes. The microstructure of the long-term measured cell was compared to that of a freshly reduced cell. Fig. 8a-c represents the fuel electrode of the reduced cell while Fig. 8d illustrates the microstructure of the corresponding oxygen electrode. Similarly, Fig. 8e-g shows the microstructure of the fuel electrode after long-term degradation test, while Fig. 8h represents the corresponding oxygen electrode. The secondary electron image of the electrode microstructure between Fig. 8a and e illustrates an increase in the Ni particle size after the degradation test. This indicates Ni particle agglomeration during CO_2 electrolysis. The Ni agglomeration is further confirmed in the backscattered electron image of Fig. 8f-g when compared to Fig. 8b-c, where gray particles are Ni and white bright particles are GDC. In addition, Ni depletion and pore formation at the electrode/electrolyte interface are also visible after the long-term degradation test as compared to the reference cell (Fig. 8a,b and e,f). The observed microstructural changes would influence the

Table 1
Possible process contribution to the polarization resistance and their corresponding frequency ranges.

Process/ Element	Frequency Range	Electrode Process
P4 (Ws)	0.3–13 Hz	diffusion process + possible surface reaction in the fuel electrode
P3 (R3)	13–110 Hz	Adsorption/desorption process + charge transfer on the fuel electrode. Surface exchange on the oxygen electrode
P2 (R2)	110–550 Hz	Ion diffusion on the oxygen electrode
P1 (R1)	550–2600 Hz	Charge transfer process across the interface (LSCF)

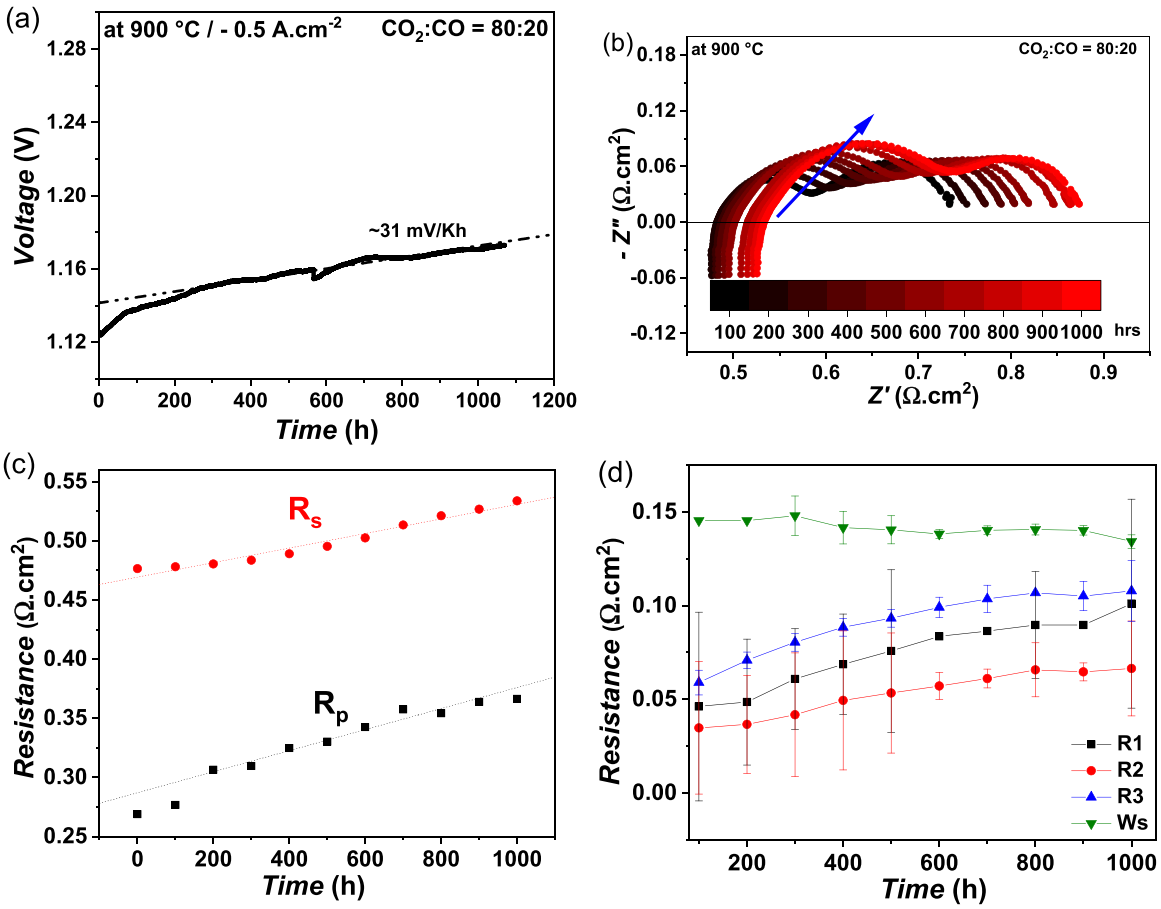

Fig. 7. a) Variation of cell voltage as a function of time, b) variation of impedance spectra (c) variation of Rs and R_p and (d) NLLS fitting results of the impedance spectra, during long-term CO_2 electrolysis test.

measured impedance result in different ways. For example, the formation of a Ni-depleted layer as a result of Ni migration away from the electrolyte increases the electrolyte thickness thereby leading to an increase in ohmic resistance, as seen in Fig. 7b. Also, Ni agglomeration would effectively reduce the active surface area for electrochemical reactions, causing an increase in polarization resistance (Fig. 7c). Lastly, the continuous progression of these effects during cell operation would inevitably result in a decrease in cell performance over time due to an increase in area specific resistance. An extensive microstructural analysis of the electrodes, in relation to the observed electrochemical degradation processes, will be the objective of another paper.

The impedance analysis also reveals that the high frequency processes, which are majorly oxygen electrode processes also contributed to the observed degradation. The secondary electron image comparison between Fig. 8d and h reveals no significant change in the LSCF microstructure. However, the mechanism of LSCF oxygen electrode degradation has been extensively studied [44–46]. One such mechanism is the formation of an insulating $SrZrO_3$ layer due to the reaction between volatile SrO and the YSZ electrolyte [44,47]. To prevent this reaction, a GDC barrier layer between the electrolyte and the oxygen electrode is adopted. However, since the GDC barrier layer in Fig. 8d and h is not fully dense, this reaction cannot be entirely prevented. Monaco et al. [47] opined that the formation of an insulating $SrZrO_3$ layer causes loss of Zr^{4+} in the 8YSZ electrolyte thereby reducing the ionic conductivity of the electrolyte and thus, leading to an increase in ohmic resistance of the cell. The increase in ohmic resistance entails a decrease in overall cell performance and thus, an increase in cell degradation [44–46].

4. Conclusion

In this study, an electrolyte-supported single cell consisting of Ni-GDC fuel electrode and LSCF oxygen electrode was fabricated and analyzed under high temperature CO_2 electrolysis conditions. Impedance measurements were carried out at different temperatures as well as under different CO_2:CO fuel gas compositions and oxygen partial pressures. The obtained impedance spectra were evaluated with both DRT and NLLS fitting. Four time constants, representing four peaks in the DRT spectra, were used to fit the impedance spectra. The high frequency P1 peak corresponds to the oxygen electrode charge transfer process while the middle frequency processes of P2 and P3 consist of contribution from surface reaction processes from both the fuel and oxygen electrodes. Lastly, the low frequency process is assigned to the gas diffusion process in addition to the surface reaction in the fuel electrode. Long-term degradation analysis was performed at 900 °C and a current density of -0.5 A·cm^{-2}. The cell shows a low degradation rate of 31 mV·kh^{-1} during 1070 h of operation. Furthermore, analysis of the degradation mechanism showed that the high/mid frequency processes contributed more to the degradation rate. Microstructural evaluation of the measured cell with SEM revealed Ni particle agglomeration, increase in electrode porosity and Ni migration away from the electrolyte.

CRediT authorship contribution statement

Ifeanyichukwu D. Unachukwu: Methodology, Investigation, Formal analysis, Validation, Conceptualization, Data curation, Software, Visualization, Writing – original draft, Writing – review & editing. **Vaibhav Vibhu:** Methodology, Formal analysis, Validation,

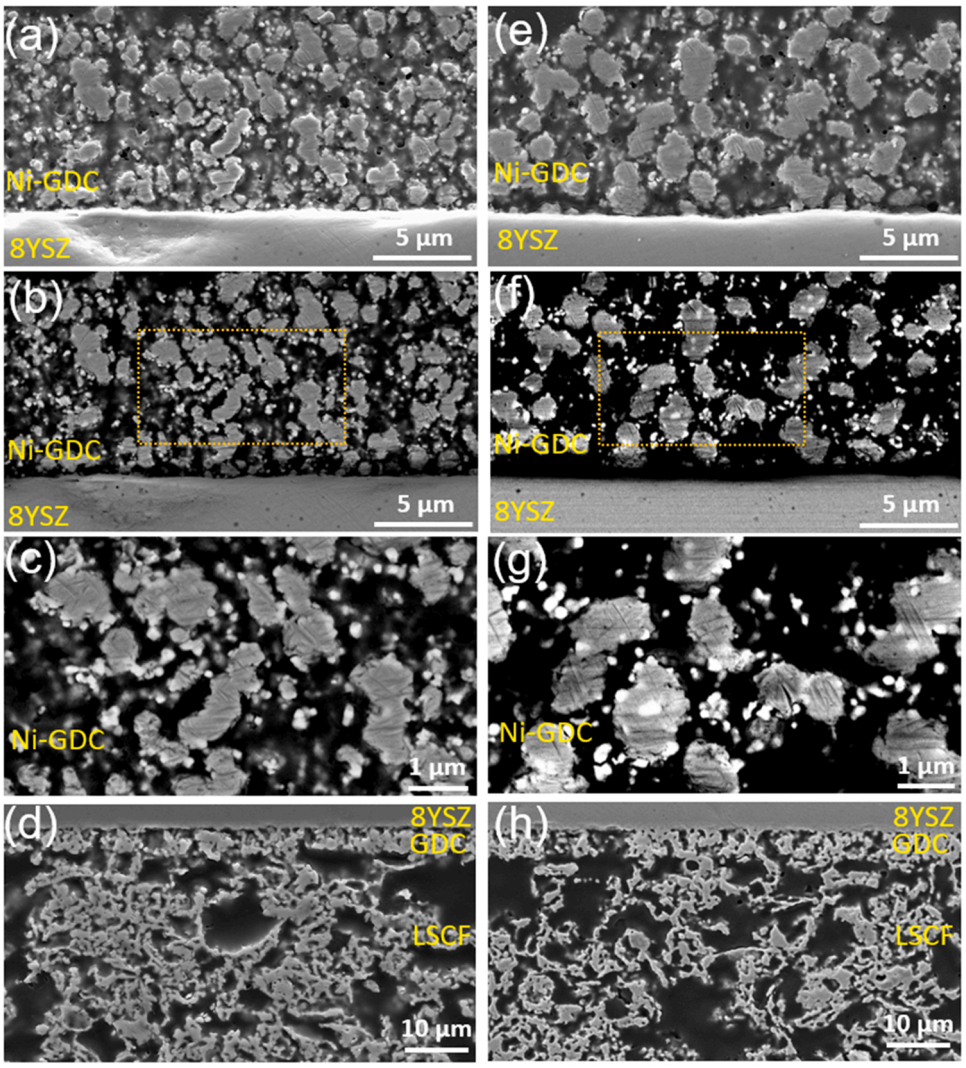

Fig. 8. SEM images of the cell microstructure. (a-d) as reduced cell (e-h) after degradation test in CO_2 electrolysis. Figures a, e, d and h were taken using a secondary electron detector, while Figures b, c, f and g were taken using a backscattered electron detector.

Conceptualization, Software, Supervision, Visualization, Writing – review & editing. **Jan Uecker:** Investigation, Formal analysis, Validation. **Izaak C. Vinke:** Methodology, Supervision, Validation, Project administration, Conceptualization, Resources, Software, Visualization. **Rüdiger-A. Eichel:** Supervision, Project administration, Resources. **L.G. J. (Bert) de Haart:** Methodology, Supervision, Validation, Project administration, Conceptualization, Resources, Software, Visualization.

Declaration of Competing Interest

The authors declare that they have no known competing financial interests or personal relationships that could have appeared to influence the work reported in this paper.

Data availability

Data will be made available on request.

Acknowledgments

The authors gratefully acknowledge funding by the German Federal Ministry of Education and Research (BMBF) within the iNEW 2.0 Project: incubator sustainable and renewable value chains, under grant agreement number 03SF0627A.

Appendix A. Supplementary material

Supplementary data associated with this article can be found in the online version at doi:10.1016/j.jcou.2023.102423.

References

[1] M. Jouny, W. Luc, F. Jiao, General techno-economic analysis of CO_2 electrolysis systems, Ind. Eng. Chem. Res. 57 (2018) 2165–2177, https://doi.org/10.1021/acs.iecr.7b03514.
[2] R.K. Pachauri, L. Mayer, Climate Change 2014: Synthesis Report, Intergovernmental Panel on Climate Change, Geneva, Switzerland, 2015.
[3] IEA, The Future of Petrochemicals – Analysis – IEA, 2022. ⟨https://www.iea.org/reports/the-future-of-petrochemicals⟩, (Accessed 2 March 2022).
[4] R. Küngas, Review—electrochemical CO2 reduction for CO production: comparison of low- and high-temperature electrolysis technologies, J. Electrochem. Soc. 167 (2020) 44508, https://doi.org/10.1149/1945-7111/ab7099.
[5] M. Ni, M. Leung, D. Leung, Technological development of hydrogen production by solid oxide electrolyzer cell (SOEC), Int. J. Hydrog. Energy 33 (2008) 2337–2354, https://doi.org/10.1016/j.ijhydene.2008.02.048.
[6] A. Nechache, S. Hody, Alternative and innovative solid oxide electrolysis cell materials: a short review, Renew. Sustain. Energy Rev. 149 (2021), 111322, https://doi.org/10.1016/j.rser.2021.111322.
[7] E.M. Sala, N. Mazzanti, M.B. Mogensen, C. Chatzichristodoulou, Current understanding of ceria surfaces for CO_2 reduction in SOECs and future prospects – a review, Solid State Ion. 375 (2022), 115833, https://doi.org/10.1016/j.ssi.2021.115833.

[8] J.A. Rabinowitz, M.W. Kanan, The future of low-temperature carbon dioxide electrolysis depends on solving one basic problem, Nat. Commun. 11 (2020) 5231, https://doi.org/10.1038/s41467-020-19135-8.

[9] M.B. Mogensen, M. Chen, H.L. Frandsen, C. Graves, A. Hauch, P.V. Hendriksen, T. Jacobsen, S.H. Jensen, T.L. Skafte, X. Sun, Ni migration in solid oxide cell electrodes: review and revised hypothesis, Fuel Cells (2021).

[10] A. Hauch, M. Mogensen, A. Hagen, Ni/YSZ electrode degradation studied by impedance spectroscopy — Effect of p(H_2O), Solid State Ion. 192 (2011) 547–551, https://doi.org/10.1016/j.ssi.2010.01.004.

[11] A. Hauch, S.D. Ebbesen, S.H. Jensen, M. Mogensen, Solid oxide electrolysis cells: microstructure and degradation of the Ni/yttria-stabilized zirconia electrode, J. Electrochem. Soc. 155 (2008) B1184–B1193, https://doi.org/10.1149/1.2967331.

[12] C. Graves, S.D. Ebbesen, S.H. Jensen, S.B. Simonsen, M.B. Mogensen, Eliminating degradation in solid oxide electrochemical cells by reversible operation, Nat. Mater. 14 (2015) 239–244, https://doi.org/10.1038/nmat4165.

[13] S.D. Ebbesen, X. Sun, M.B. Mogensen, Understanding the processes governing performance and durability of solid oxide electrolysis cells, Faraday Discuss. 182 (2015) 393–422, https://doi.org/10.1039/c5fd00032g.

[14] V. Alzate-Restrepo, J.M. Hill, Carbon deposition on Ni/YSZ anodes exposed to CO/H_2 feeds, J. Power Sources 195 (2010) 1344–1351, https://doi.org/10.1016/j.jpowsour.2009.09.014.

[15] H. He, J.M. Hill, Carbon deposition on Ni/YSZ composites exposed to humidified methane, Appl. Catal. A Gen. 317 (2007) 284–292, https://doi.org/10.1016/j.apcata.2006.10.040.

[16] Y. Tao, S.D. Ebbesen, M.B. Mogensen, Carbon deposition in solid oxide cells during Co-electrolysis of H_2O and CO_2, J. Electrochem. Soc. 161 (2014) F337–F343, https://doi.org/10.1149/2.079403jes.

[17] Y. Song, Z. Zhou, X. Zhang, Y. Zhou, H. Gong, H. Lv, Q. Liu, G. Wang, X. Bao, Pure CO_2 electrolysis over an Ni/YSZ cathode in a solid oxide electrolysis cell, J. Mater. Chem. A 6 (2018) 13661–13667, https://doi.org/10.1039/C8TA02858C.

[18] Z.A. Feng, M.L. Machala, W.C. Chueh, Surface electrochemistry of CO_2 reduction and CO oxidation on Sm-doped $CeO_{(2-x)}$: coupling between $Ce^{(3+)}$ and carbonate adsorbates, Phys. Chem. Chem. Phys. 17 (2015) 12273–12281, https://doi.org/10.1039/c5cp00114e.

[19] Y. Yu, B. Mao, A. Geller, R. Chang, K. Gaskell, Z. Liu, B.W. Eichhorn, CO_2 activation and carbonate intermediates: an operando AP-XPS study of CO_2 electrolysis reactions on solid oxide electrochemical cells, Phys. Chem. Chem. Phys. 16 (2014) 11633–11639, https://doi.org/10.1039/C4CP01054J.

[20] D. Chen, M. Barreau, S. Turczyniak-Surdacka, K. Sobczak, M. Strawski, A.G. Le Salle, A. Efimenko, D. Teschner, C. Petit, S. Zafeiratos, Ceria nanoparticles as promoters of CO_2 electroreduction on Ni/YSZ: an efficient preparation strategy and insights into the catalytic promotion mechanism, Nano Energy 101 (2022), 107564, https://doi.org/10.1016/j.nanoen.2022.107564.

[21] P. Courty, H. Ajot, C. Marcilly, B. Delmon, Oxydes mixtes ou en solution solide sous forme très divisée obtenus par décomposition thermique de précurseurs amorphes, Powder Technol. 7 (1973) 21–38, https://doi.org/10.1016/0032-5910(73)80005-1.

[22] Overview – NORECS, 2022. ⟨https://www.norecs.com/index.php?page=Overview⟩, (Accessed 18 August 2022).

[23] S. Foit, L. Dittrich, T. Duyster, I. Vinke, R.-A. Eichel, L.G.J. de Haart, Direct solid oxide electrolysis of carbon dioxide: analysis of performance and processes, Processes 8 (2020) 1390, https://doi.org/10.3390/pr8111390.

[24] B. Boukamp, Practical application of the Kramers-Kronig transformation on impedance measurements in solid state electrochemistry, Solid State Ion. 62 (1993) 131–141, https://doi.org/10.1016/0167-2738(93)90261-Z.

[25] H. Sumi, T. Yamaguchi, K. Hamamoto, T. Suzuki, Y. Fujishiro, T. Matsui, K. Eguchi, AC impedance characteristics for anode-supported microtubular solid oxide fuel cells, Electrochim. Acta 67 (2012) 159–165, https://doi.org/10.1016/j.electacta.2012.02.021.

[26] M. Athanasiou, D.K. Niakolas, S. Bebelis, S.G. Neophytides, Steam effect on Gerischer impedance response of a Ni/GDC|YSZ|LSM fuel cell / anode, J. Power Sources 448 (2020), 227404, https://doi.org/10.1016/j.jpowsour.2019.227404.

[27] G. Nurk, T. Huthwelker, A. Braun, C. Ludwig, E. Lust, R. Struis, Redox dynamics of sulphur with Ni/GDC anode during SOFC operation at mid- and low-range temperatures: an operando S K-edge XANES study, J. Power Sources 240 (2013) 448–457, https://doi.org/10.1016/j.jpowsour.2013.03.187.

[28] H. Kan, H. Lee, Enhanced stability of Ni–Fe/GDC solid oxide fuel cell anodes for dry methane fuel, Catal. Commun. 12 (2010) 36–39, https://doi.org/10.1016/j.catcom.2010.07.014.

[29] D.A. Macedo, F.M. Figueiredo, C.A. Paskocimas, A.E. Martinelli, R.M. Nascimento, F.M. Marques, Ni–CGO cermet anodes from nanocomposite powders: Microstructural and electrochemical assessment, Ceram. Int. 40 (2014) 13105–13113, https://doi.org/10.1016/j.ceramint.2014.05.010.

[30] F. Kundracik, M. Hartmanová, J. Müllerová, M. Jergel, I. Kostič, R. Tucoulou, Ohmic resistance of thin yttria stabilized zirconia film and electrode–electrolyte contact area, Mater. Sci. Eng. B 84 (2001) 167–175, https://doi.org/10.1016/S0921-5107(01)00515-3.

[31] B.A. Boukamp, Derivation of a distribution function of relaxation times for the (fractal) finite length warburg, Electrochim. Acta 252 (2017) 154–163, https://doi.org/10.1016/j.electacta.2017.08.154.

[32] Y. Zhang, Y. Chen, M. Yan, F. Chen, Reconstruction of relaxation time distribution from linear electrochemical impedance spectroscopy, J. Power Sources 283 (2015) 464–477, https://doi.org/10.1016/j.jpowsour.2015.02.107.

[33] A. Leonide, SOFC modeling and parameter identification by means of impedance spectroscopy, Meet. Abstr. (2009), https://doi.org/10.1149/MA2009-01/42/1439.

[34] W.G. Bessler, Gas concentration impedance of solid oxide fuel cell anodes: 1 Stagnation point flow geometry, J. Electrochem. Soc. 153 (2006) A1492–A1504.

[35] W.G. Bessler, S. Gewies, Bessler_2007_gas concentration impedance of solid oxide fuel cell anodes-II. Channel geometry, J. Electrochem. Soc. 156 (6) (2007) B548–B559.

[36] D.A. Osinkin, N.M. Bogdanovich, A.L. Gavrilyuk, Rate determining steps of fuel oxidation over CeO_2 impregnated Ni-YSZ in H_2+ H_2O + CO + CO_2 ambient, Electrochim. Acta 199 (2016) 108–115, https://doi.org/10.1016/j.electacta.2016.03.133.

[37] R. Green, C. Liu, S. Adler, Carbon dioxide reduction on gadolinia-doped ceria cathodes, Solid State Ion. 179 (2008) 647–660, https://doi.org/10.1016/j.ssi.2008.04.024.

[38] J. Kim, D. Shin, J.-W. Son, J.-H. Lee, B.-K. Kim, H.-J. Je, H.-W. Lee, K.J. Yoon, Fabrication and characterization of all-ceramic solid oxide fuel cells based on composite oxide anode, J. Power Sources 241 (2013) 440–448, https://doi.org/10.1016/j.jpowsour.2013.04.139.

[39] H. Watanabe, A. Unemoto, K. Amezawa, T. Kawada, Electrochemical analysis on degradation of Ni-GDC cermet anode for SOFC, ECS Trans. 25 (2009) 1939–1944, https://doi.org/10.1149/1.3205738.

[40] A. Leonide, B. Rüger, A. Weber, W.A. Meulenberg, E. Ivers-Tiffée, Impedance Study of Alternative (La,Sr)FeO3−δ and(La,Sr)(Co,Fe)O3−δ MIEC Cathode Compositions, 157(2), 2010, pp. B234–B239.

[41] D. Papurello, D. Menichini, A. Lanzini, Distributed relaxation times technique for the determination of fuel cell losses with an equivalent circuit model to identify physicochemical processes, Electrochim. Acta 258 (2017) 98–109, https://doi.org/10.1016/j.electacta.2017.10.052.

[42] Y. Chen, Y. Bu, Y. Zhang, R. Yan, D. Ding, B. Zhao, S. Yoo, D. Dang, R. Hu, C. Yang, M. Liu, A highly efficient and robust nanofiber cathode for solid oxide fuel cells, Adv. Energy Mater. 7 (2017), 1601890, https://doi.org/10.1002/aenm.201601890.

[43] V. Yurkiv, R. Costa, Z. Ilhan, A. Ansar, W.G. Bessler, Impedance of the surface double layer of LSCF/CGO composite cathodes: an elementary kinetic model, J. Electrochem. Soc. 161 (2014) F480–F492, https://doi.org/10.1149/2.070404jes.

[44] V. Vibhu, I.C. Vinke, F. Zaravelis, S.G. Neophytides, D.K. Niakolas, R.-A. Eichel, L.G.J. de Haart, Performance and degradation of electrolyte-supported single cell composed of Mo-Au-Ni/GDC fuel electrode and LSCF oxygen electrode during high temperature steam electrolysis, Energies 15 (2022) 2726, https://doi.org/10.3390/en15082726.

[45] N. Sakai, H. Kishimoto, K. Yamaji, T. Horita, M.E. Brito, H. Yokokawa, Degradation behavior at interface of LSCF cathodes and rare earth doped ceria, ECS Trans. 7 (2007) 389–398, https://doi.org/10.1149/1.2729115.

[46] S.P. Simner, M.D. Anderson, M.H. Engelhard, J.W. Stevenson, Degradation mechanisms of La–Sr–Co–Fe–O_3 SOFC cathodes, Electrochem. Solid State Lett. 9 (2006).

[47] F. Monaco, D. Ferreira-Sanchez, M. Hubert, B. Morel, D. Montinaro, D. Grolimund, J. Laurencin, Oxygen electrode degradation in solid oxide cells operating in electrolysis and fuel cell modes: LSCF destabilization and interdiffusion at the electrode/electrolyte interface, Int. J. Hydrog. Energy 46 (2021) 31533–31549, https://doi.org/10.1016/j.ijhydene.2021.07.054.